Research Square

Preprints are preliminary reports that have not undergone peer review.
They should not be considered conclusive, used to inform clinical practice,
or referenced by the media as validated information.

Cooperative Reconstructive Epitaxy of MoS2 Monolayers in a Multi-Wafer MOCVD Process Guided by In-Situ Process Monitoring

David Estrada

daveestrada@boisestate.edu

Boise State University https://orcid.org/0000-0001-5894-0773

Michael Curtis

Boise State University

Mayukh Das

Penn State University

Merve Baksi

Tufts University

Stiven Forti

Italian Institute of Technology Pisa

Antonio Rossi

Italian Institute of Technology Pisa

Li-Syuan Lu

Penn State University

Daniel Sanchez

Boise State University

Danilo Nagaoka

Penn State University

Tony Valayil Varghese

Boise State University https://orcid.org/0000-0002-3251-8395

Kurt Eyink

Air Force Research Labs

Ly Tran

Air Force Research Labs

Krishnendu Mukhopadhyay

Penn State University

Mangesh Diware

Park Systems

Ashton Enrriques

Park Systems
Nick Glavin
Air Force Research Labs
Christof Mauder
AIXTRON SE
Alexander Henning
AIXTRON SE
Mauricio Terrones
The Pennsylvania State University
Joshua Robinson
Penn State University
Paul Simmonds
Tufts University
Camilla Coletti
Italian Institute of Technology https://orcid.org/0000-0002-8134-7633
Salim El Kazzi
AIXTRON SE
Saptarshi Das
Penn State University https://orcid.org/0000-0002-0188-945X

Article

Keywords:

Posted Date: June 5th, 2026

DOI: https://doi.org/10.21203/rs.3.rs-9909957/v1

License: This work is licensed under a Creative Commons Attribution 4.0 International License.
Read Full License

Additional Declarations: There is **NO** Competing Interest.

Cooperative Reconstructive Epitaxy of MoS_2 Monolayers in a Multi-Wafer MOCVD Process Guided by In-Situ Process Monitoring

Michael Curtis[1], Mayukh Das[2], Merve Baksi[3], Stiven Forti[4], Antonio Rossi[4], Li-Syuan Lu[5], David Sanchez[6], Danilo Nagaoka[6], Tony Valayil Varghese[1], Kurt Eyink[7], Ly D. Tran[7], Krishnendu Mukhopadhyay[2], Mangesh Diware[8], Ashton Enrriques[8], Nick Glavin[7], Christof Mauder[9], Alexander Henning[9], Mauricio Terrones[6], Joshua Robinson[5], Paul J. Simmonds[3], Camilla Coletti[4], Salim El Kazzi[9], Saptarshi Das[10], David Estrada[1,*]

1. Micron School of Materials Science and Engineering, Boise State University, Boise, ID, 83725
2. Engineering Science and Mechanics, The Pennsylvania State University, University Park, PA 16802
3. Electrical & Computer Engineering, Tufts University, Medford, MA 02155
4. Center for Nanotechnology Innovation, Istituto Italiano di Tecnologia, Piazza San Silvestro 12, Pisa, 56127, Italy
5. Materials Science and Engineering, The Pennsylvania State University, University Park, PA 16802
6. Department of Physics, The Pennsylvania State University, University Park, PA, 16802
7. Air Force Research Laboratory, Materials and Manufacturing Directorate, Wright-Patterson Air Force Base, Ohio 45433
8. Park Systems Inc., Burlington, MA 01803
9. AIXTRON SE, Dornkaulstr 2, 52134 Herzogenrath, Germany
10. Department of Materials Science and Engineering, The Pennsylvania State University, University Park, PA, 16802
**Corresponding Author: daveestrada@boisestate.edu*

Abstract

Two-dimensional transition metal dichalcogenides (TMDs) are promising for scaled electronic and optoelectronic technologies, yet wafer-scale MOCVD growth remains limited by challenges in crystalline uniformity, layer-number control, and reproducibility. Here we report an industry-scalable multi-wafer MOCVD process in which a post-deposition anneal (PDA) induces a cooperative reconstructive epitaxy mechanism between the sapphire substrate and the as-grown MoS_2 monolayer. The PDA transforms the native ~0.2 nm monostep sapphire morphology into uniform double steps, yielding an epitaxial, single-crystal MoS_2 monolayer in van der Waals contact with the reconstructed surface and exhibiting reduced point and line defect densities. Electrical measurements from 100 back-gated nanoscale transistors demonstrate wafer-scale reproducibility, with mobilities up to 45 $cm^2 V^{-1} s^{-1}$. Guided by in-situ photoreflectance monitoring, we establish a modular, transferable growth sequence optimized for MoS_2 and extensible to WS_2, $MoSe_2$, and WSe_2, providing a practical route toward commercial-grade, wafer-scale TMD synthesis.

1. Introduction

Monolayer TMDs are potential solutions to current pressing technological challenges. Their high theoretical mobility, direct bandgaps from the visible to near IR range, and atomically thin geometry

make them compelling candidates for next-generation electronic and optoelectronic devices[1–4]. The International Roadmap for Devices and Systems projects the integration of 2D TMD based technologies as silicon complements, and possibly beyond silicon applications, by the end of the decade[5]. TMD thin films have been synthesized by both top-down and bottom-up processes for various uses[6–13]. While solution processed materials are a good fit for thin-film transistors and printed electronic devices, they are not suitable for integration with high volume wafer scale manufacturing of CMOS-based computing architectures. In high volume manufacturing, vapor deposition techniques provide the necessary scaling and throughput for commercial applications. Among them, metalorganic chemical vapor deposition (MOCVD) is suitable for deposition of highly crystalline semiconducting material systems, including the 2D family of materials. This field of TMD research that began modestly, synthesis through isolation of atomic layers by micromechanical exfoliation, is now the target of industrial MOCVD process integration efforts[14–26] where material quality, wafer scale uniformity and multi-wafer scalability are essential. A successful process must also integrate seamlessly into existing production lines with sufficient instrumentation to drive statistical process control (SPC) without introducing excessive processing steps.

Despite advances, achieving wafer-scale single-crystal monolayers in a manufacturing-relevant MOCVD environment remains an open challenge. Recently, refinement of the 2D TMD MOCVD and CVD processes has included pre-growth optimization of the preferred epitaxial substrate, crystalline Al_2O_3, or sapphire [27–34]. The evolution of the sapphire surface during deposition processes is a known source of defects in the TMD layers above[35,36]. Step-edge guided epitaxy is one method for obtaining unidirectional domains of monolayer TMDs[29,30,34,37]. In this growth mechanism, alignment of the sapphire step edge initiates nucleation and guides lateral growth towards coalescence (referred to as step-flow growth)[38–40]. Another method for obtaining unidirectional monolayers is through van der Waals (vdW) epitaxy onto optimized sapphire surfaces[30,33,41–43]. In contrast to step-flow growth, nucleation occurs on the basal plane of the terrace steps, as well as their edges, and growth continuous to full coalescence.

In this work we report the multi-wafer growth of single crystal MoS_2 monolayers in an industry-relevant MOCVD system (**Figure 1**) guided by *in-situ* process monitoring and enabled through a cooperative reconstructive vdW epitaxy mechanism. Sapphire with an industry standard cost-effective 0.2° c/m offcut is used as the growth substrate. We have discovered that sapphire surface reconstruction occurs simultaneously with precursor delivery and post-processing in a single and continuous MoS_2 MOCVD run, a process we describe as cooperative reconstructive epitaxy. We discuss preliminary results on the universality of this approach by translating the recipe for MoS_2 to WS_2, WSe_2, and $MoSe_2$. Back-gated nanoscale transistors are fabricated to elucidate the electrical transport properties of these TMD films, with the best MoS_2 devices exhibiting carrier mobilities up to ~45 $cm^2V^{-1}s^{-1}$. This cooperative

reconstructive epitaxy framework provides a scalable pathway towards multi-wafer single-crystal TMD monolayer growth and potential integration into existing semiconductor manufacturing workflows.

2. Results and Discussion

2.1 Sapphire Annealing

Sapphire annealing is ubiquitous in TMD CVD and MOCVD growth literature. This step exists to clean the as-purchased substrates, reveal the characteristic terrace morphology, and passivate the surface by means of the hydride chalcogen precursor[33,44,45]. **Supplementary Figure 1** displays the results of a temperature series annealing study on c-plane sapphire with and without the injection of H_2S as the hydride chalcogen precursor. At 700° C, the as-purchased sapphire shows no visible surface structure for either H_2 and H_2/H_2S anneals. At 800° C, jagged terraces become visible as the sapphire is etched. By 900° C, both samples have visible terraces, but in contrast with the sample annealed under H_2 alone, the terrace edges of the sample annealed under H_2/H_2S smooth slightly. At 1000° C, both samples show evidence of edge smoothing, but again with the sample exposed to H_2/H_2S appearing slightly smoother. This annealing study, combined with reports from the CVD literature that sapphire is stable below 900 °C, was used as the basis for the quenching step described in *Methods*[46–49].

We use reflection high-energy electron diffraction (RHEED) to establish a reliable in-plane calibration of the α-Al_2O_3 (0001) substrate. Following annealing under H_2, RHEED patterns acquired along the $[11\bar{2}0]$ azimuth only exhibit integer-order streaks, with no observable fractional-order features, consistent with an unreconstructed (1×1) sapphire surface (**Supplementary Figures 2a–b**). Identical, unreconstructed RHEED patterns were also observed for α-Al_2O_3 (0001) substrates annealed under H_2/H_2S (**Supplementary Figures 2c–d**). Along the $[11\bar{2}0]$ azimuth (**Supplementary Figures 2a, 2c**), we index the streak spacing across multiple measurements to an in-plane lattice parameter of approximately 4.78 Å, which corresponds closely to the hexagonal surface net of sapphire. Upon rotation of the substrate by 30° to the $[10\bar{1}0]$ azimuth (**Supplementary Figures 2b, 2d**), steak spacing increases by a factor of $\sqrt{3}$, consistent with the geometry of sapphire along the direction normal to the m-plane. RHEED patterns. The RHEED patterns in **Supplementary Figures 2a–d** then repeat every 60° as the sample is rotated as expected from the hexagonal symmetry of the c-plane sapphire surface.

2.2 MOCVD Process

We adopted the multistep approach consisting of nucleation, ripening and growth stages. The temperature is bounded by a maximum of 850° C while metal precursor is actively flowing, and portions of the sapphire surface remain uncovered. The rationale for this process was to focus on protecting the sapphire substrate during growth and anneal out defects once sufficient precursor material had been

delivered to the surface. **Figure 2** shows the evolution of the sample surface from nucleation to growth and *in-situ* post-deposition annealing (PDA) as measured by AFM. **Figure 2a** reveals that the MoS_2 nucleation is not edge guided, with small domains densely dispersed across the terrace surfaces. This is the first indication that MoS_2 growth is not taking place in the step-flow growth regime. In **Figure 2b,** deposition of one monolayer of MoS_2 has reached its endpoint as measured by in-situ photoreflectance (**Supplementary Figure 3**). The surface morphology is rough with some points of vertical development and a suggestion of inhomogeneity in the sapphire surface below. However, after the the PDA, the monolayer surface transitions from the morphology in **Figure 2b** to that seen in **Figure 2c**. At this point the homogenous sapphire terraces become clearly visible underneath the uniform MoS_2 monolayer. Minimal bilayers MoS_2 domains are seen.

2.3 Cooperative Reconstructive Epitaxy on Standard C-Plane Sapphire

Crystalline sapphire is the TMD growth substrate of choice in many CVD/MOCVD applications. In its most common form, the bulk crystal is cleaved orthogonally to its c-plane axis, traditionally with a controlled off-cut, i.e. a tilt towards the m plane direction of a few tenths of a degree. This form of sapphire is widely used in the III-V semiconductor industry, where decades of use has driven supply chain maturity and low substrate costs [50]. Its compatibility with existing manufacturing processes provides a clear economic advantage for scalable integration over more specialized/engineered sapphire substrates[51].

The bulk unit cell of c-plane (0001) Al_2O_3 has a trigonal symmetry and consists of repeating 6 layers in an ABABAB stack structure[52]. The c_0 lattice parameter has a length of approximately 12.982 Å, giving each slab a thickness of $c_0/6 = 2.16$ Å[53]. These alternating "A" and "B" surfaces are revealed during both the H_2 and H_2/H_2S annealing treatments we describe previously. A schematic representation of the sapphire structure and these A, B oxygen references are shown in **Figure 2e**. An important characteristic about the A and B surfaces is their mirror symmetry about the terrace edge. The alternation of these chiral A and B terminations results in preferential growth of TMD domains with opposing orientations on adjacent terraces. As a result, the surface exhibits two energetically equivalent, symmetry-related domain configurations overall, giving rise to antiparallel TMD domain alignment during growth[41,54]. In contrast, elimination of this terrace-to-terrace alternation would enable the growth of TMDs with a single orientation and interfacial termination across the entire sapphire surface, lifting this orientational degeneracy and enabling large area unidirectional TMD domain alignment.[42,55]. Short of constructing a perfect sapphire basal plane and maintaining it during growth, the next best option for TMD growth would be to generate a uniformly double stepped surface consisting of only A or B sapphire layers from the (0001) bulk Al_2O_3 unit cell *ex-situ*. It was previously demonstrated by both CVD and MOCVD techniques that *ex-situ* annealing could enable TMD orientation control, particularly when using

off-cut sapphire substrates where one can control the terrace widths [19,35,42,43,56]. From this perspective, it has been argued that standard, nominally on-axis c- or m-plane sapphire is not appropriate for this type of symmetry-driven domain control[34].

Our work stands apart from similar MOCVD-based results in that from nucleation to full monolayer coverage of MoS_2 the surface exhibits a uniform monostepped terrace structure, as shown in **Figures 2a,b** and indicated by in- situ photoreflectance[35,43]. However, PDA post-growth treatment produces a significant change in the surface morphology (**Figure 2c**). We analyze the surfaces before growth and after MoS_2 growth/PDA by counting step heights on the samples from XZ line scans. Prior to growth the results indicate predominantly single steps are present on the substrate surface representing alternating oxygen-terminated A and B layers (A/B surface), with a thickness of ~0.2 nm, correct for a monolayer step on the sapphire surface[42]. After MoS_2 growth, PDA and process completion, the average step height increases to ~0.4 nm, indicating that the sapphire single steps have developed into double steps, consistent with an A/A (or B/B) layer terminated surface. The slight loss of height relative to the known height of sapphire double steps is attributed to interactions between the AFM probe and the existing TMD monolayer that is in van der Waals contact with the sapphire surface[31,57,58].

Importantly, sapphire substrates used for our growths were loaded into the MOCVD reactor as purchased without any *ex-situ* pretreatment. The growth temperature ceiling is intentionally chosen to keep the sapphire surface stable until after deposition of the TMD[49]. Upon application of the PDA, the sapphire surface and overlayed TMD monolayer appear to ***cooperatively reconstruct***. The sapphire, transitioning into uniform double steps, and the MoS_2 layer above healing grain boundaries, point defects, and improving unidirectional domain alignment.

Figure 3 presents the results of cross-sectional TEM and EDS of the single atomic layer of MoS_2 deposited on the sapphire substrate. The space between the MoS_2 and sapphire in **Figure 3a** is attributed to a vdW buffer layer. In **Figure 3d** shows the monolayer TMD draping over a sapphire double step with a measured step height of 0.44 nm which is appropriate for a double step of sapphire. As the layer approaches the terrace edge, it appears that the buffer layer thickness is reduced slightly. Raw TEM cross-sections are available in **Supplementary Figure 4**. The elemental distribution across the MoS_2/sapphire interface was explored with EDS mapping. Mo (**Figure 3b**) and S (**Figure 3c**) signals are localized to a narrow band at the interface as would be expected for a uniform monolayer. There is no evidence of significant interdiffusion into the substrate. The signals for Al and O (**Figure 3e/f**) are confined to the region below the monolayer, again with no signs of interdiffusion up into the monolayer. Together with the TEM data, these results support the formation of a chemically pure monolayer in vdW contact with the sapphire.

The sapphire double step formation in this process is not the result of time or temperature alone. **Supplementary Figure 5a** shows the results of a sapphire wafer exposed to an extended version of the 1000° C pretreatment, with the hydride anneal step changed from 15 to 45 minutes. Step bunching beyond a double step is clearly visible. Raising the pretreatment temperature to 1100°C at the standard time (30 min) has a similar result as the extended time at 1000° C (**Supplementary Figure 5b**). At 1200°C temperatures, long range terrace order is lost (**Supplementary Figure 5c**).

Studies into controlling step bunching on c-plane sapphire through *ex-situ* annealing found that uniform double steps could be accomplished in oxygen-containing ambient environments under conditions that typically exceeding the 1000 °C temperature of our in-situ process or took several hours at lower temperatures[33,42,59]. These ex-situ anneals can also result in a $\left(\sqrt{31}\, x\, \sqrt{31}\right)$ R9 aluminum-rich sapphire surface reconstruction[36,60,61]. In the context of this work, reconstruction strictly refers to the modification of the sapphire steps. RHEED analysis of MoS_2-on-sapphire samples (described later) indicates that the sapphire retains an unreconstructed $(1\ x\ 1)$ surface throughout our process. To our knowledge this is the first demonstration of a controlled *in-situ* terrace reconstruction of this type occurring concurrently with the reconstruction of the overlying TMD layer. The difference in morphology between the sapphire under the MoS_2 monolayer and sapphire annealed alone in this study and others suggests that the growing MoS_2 layer plays a role in regulating the sapphire surface reconstruction. Our process achieves similar results in a single continuous process within a single tool[42]. It has also been reported that MoS_2 layer number can be controlled by deliberate sapphire step bunching[32]. Interestingly, in our MoS_2 study, the small regions of bilayer deposition predominantly occur at points where there is a disturbance in the sapphire terrace edge below.

2.4 Characterization of the MoS_2 monolayer

Due to the roughness in the TMD layer prior to PDA (**Figure 2b)**, it is difficult to assess the state of the sapphire surface below. There are also no features in the topography alone that give an idea of what the grain size might be. We therefore used C-AFM to investigate the presence and nature of any grain boundaries in the MoS_2 monolayer before and after PDA (**Figure 4**). **Figure 4a** shows the topography collected concurrently with the map of current response for a monolayer of MoS_2 prior to the PDA. The MoS_2 surface exhibits a somewhat granular appearance overlaid on wavy, meandering terraces of the sapphire surface. We do not observe any of the characteristic hexagonal or triangular shapes typically seen in TMD growth[62]. The colocalized current map in **Figure 4b** reveals a prevalence of linear features where the current is high, expected to indicate high angle grain boundaries between coalesced domains of the MoS_2 due to a metallic nature of high angle grain boundaries in monolayer TMDs. However, following PDA treatment the sample surface topography is very smooth with evenly spaced terraces of

uniform height and width (**Figure 4c**). Current maps of the MoS_2 film contain no linear features associated with domain boundaries, although there is still some current variation extending out from the terrace edges (**Figure 4d**). We believe that this variation in current signal is due to changes in the thickness of the vdW buffer region separating the MoS_2 monolayer from the sapphire substrate, as depicted in **Figure 3d,** although at this time we are uncertain what degree of separation gives rise to the difference in current measured. Together with changes to the sapphire terrace morphology, the PDA seems to promote the healing of grain boundaries in the TMD monolayer, with the increased temperature of this step driving grain boundary diffusion. As part of the C-AFM study, we assessed the conductivity MoS_2 layers before and after PDA treatment by applying equal bias voltages. Under these conditions, the MoS_2 monolayer that received the PDA conducts 17× higher current than the MoS_2 sample without a PDA treatment (**Supplementary Figure 6**), believed to be a result of the increased crystallinity and thereby less scattering.

Plane view TEM images of MoS_2 monolayers growth with and without the PDA step confirm the findings of the CAFM study. **Figure 5** provides a direct comparison of grain size and domain orientation between these two films. The SAED pattern form the untreated monolayer indicates significant misorentation amongst constituent grains. The contrast in the dark field TEM images in **Figure 5b/c** allows for a visualization of the grain structure. There is a predominate grain direction, represented by the medium grey region. The slightly lighter grey regions are attributed to antiparallel domains while the darker regions are attributed to grains with an off axis misorentation relative to the prevailing grain orientation. In **Figure 5d-f**, there are no visible grain boundaries and the SAED pattern is exceedingly sharp for the film grown with a PDA treatment. The one contrasted feature in the darkfield is also present in the inset brightfield image and is attributed to a bilayer region, for which it has an appropriate morphology. Based on the results of this study reinforcing the CAFM we conclude that the cooperative reconstruction yields a single crystal monolayer. Dark field images from $[11\bar{2}0]$ spots for the layer lacking a PDA are available in **Supplementary Figure 7**.

Figure 6 provides spectroscopic and diffractive measures of MoS_2 quality. Wafer uniformity is assessed though imaging spectroscopic ellipsometry (ISE) and Raman spectroscopy measurements at wafer center, half radius, and wafer edge (**Figure 6a**). These measurements show that the MoS_2 has a uniform thickness of 0.65 nm across the entire sample surface, in good agreement with the expected value for monolayer MoS_2[63]. Analyses of Raman spectra support the monolayer assessment with equal spacing (~Δ19 cm^{-1}) of the in-plane and out-of-plane vibrational modes at the three measurement points[64–67]. The lack of any disorder-induced longitudinal acoustic Raman modes around223 cm^{-1} is indicative of a high-quality layer[68]. The absence of peaks related to graphitic or amorphous carbon in Raman spectra taken out

to 1800 cm^{-1} confirms that carbon does not incorporate into the MoS_2 monolayer during MOCVD growth (**Supplementary Figure 8a**)[24]. Photoluminescence spectra from MoS_2 monolayers before and after PDA both show expected signals from the neutral exciton and negatively charged trion (**Figure 6b**). However, the PL peak from the sample that did not undergo PDA has an appreciable low-energy shoulder, which is associated with a higher defect density [69,70].

X-ray photoelectron spectroscopy (XPS) reveals any stoichiometric differences between MoS_2 samples before and after a PDA (**Figure 6c**). Although XPS results from survey scans of the respective MoS_2 monolayers are very similar, high-resolution S 2p spectra do show some important differences. There is a noticeably stronger Mo-O-S contribution to the model fit in the sample that did not receive a PDA. This contribution is expected to come from the oxidation of sulfur vacancies in the TMD basal plane upon contact with room air[71–73]. The weaker Mo-O-S contribution in the XPS from the MoS_2 film that underwent PDA show that less oxidation occurred upon removal from the MOCVD system. It therefore appears that the PDA process helps to improve crystal quality by healing sulfur vacancy point defects in as-grown MoS_2 monolayer films.

In-plane XRD measurements of the MoS_2 films show strong epitaxial registry with the Al_2O_3 with a single in-plane orientation with no rotated variants (**Figure 6d**). When comparing the Φ scans of MoS_2 layers that before/after PDA, the azimuthal FWHM width is considerably narrower for the MoS_2 sample that underwent PDA (0.17° compared with 1.68º), indicating that the PDA improves directional uniformity of the MoS_2 domains. Grazing incidence XRD measurements show only the expected in-plane reflections of the hexagonal 2H TMD phase. There are no additional peaks attributed to oxides or phase polytypes (**Supplementary Figure 8b**).

Complementary low-energy electron diffraction (LEED) measurements on MoS_2 monolayer films that received a PDA as part of their growth exhibit a well-defined threefold symmetric diffraction pattern characteristic of MoS_2, confirming long-range crystalline order and a single in-plane orientation on the sapphire substrate (**Figure 6e**). The sharpness and symmetry of the diffraction spots indicate high structural quality and coherent epitaxial alignment of the film.

We probed the near-surface electronic structure of PDA treated MoS_2 monolayers using angle-resolved photoemission spectroscopy (ARPES) measurements to resolve both valence and conduction band edges (**Figure 6f**). To simultaneously resolve the strong valence band features and the much weaker spectral weight associated with the conduction band onset, the data were processed using a curvature analysis method, which is analogous to taking the second derivative of the ARPES intensity map[74]. This approach enhances features and improves contrast. The resulting dispersion along the Γ–K direction clearly resolves the upper valence band maximum at K, while a faint but discernible increase in intensity

near the Fermi level at K indicates the onset of the conduction band. The presence of this feature is consistent with the expected direct bandgap character at the K point for monolayer 2H-MoS_2.

RHEED patterns acquired after the growth/PDA of the MoS_2 monolayer confirm an epitaxial relation between $[11\bar{2}0]$ MoS_2 (0001) and the underlying $[11\bar{2}0]$ α-Al_2O_3 (0001) substrate (**Supplementary Figure 2**). The diffraction patterns from the MoS_2 monolayer include both brighter and weaker sets of streaks. Along the $[11\bar{2}0]$ azimuth, bright streaks attributed to the MoS_2 overlayer yield an in-plane lattice parameter of approximately 3.15 Å when indexed against the sapphire calibration, consistent with reported values for monolayer MoS_2[63] (**Supplementary Figure 2e**). Upon rotation to the $[10\bar{1}0]$ azimuth, the MoS_2 streak spacing decreases to approximately 1.82 Å (**Supplementary Figure 2f**), corresponding to the expected $a/\sqrt{3}$ row spacing of the MoS_2 lattice at in this direction, further confirming correct azimuthal assignment and internal consistency of the indexing. In addition to the primary MoS_2 features, weaker intermediate diffraction features are observed for both azimuths at larger real-space periodicities than associated with either lattice alone (9.45 Å and 5.57 Å for $[11\bar{2}0]$ and $[10\bar{1}0]$ respectively). These features are consistent with a $(3\ x\ 3)$ 2H-MoS_2 (0001) over $(2\ x\ 2)$ α-Al_2O_3 (0001) coincidence superlattice, rather than from a reconstructed sapphire surface. The absence of fractional-order substrate streaks associated with known sapphire reconstructions, together with the correct MoS_2 lattice parameters and their $1/\sqrt{3}$ scaling between azimuths, indicates a well-ordered, epitaxially aligned monolayer film over a $(1\ \times\ 1)$ sapphire surface.

2.5 Device Performance

For electrical evaluation of the wafer-scale monolayer MoS_2 grown by MOCVD, we fabricated field-effect transistors (FETs) from MoS_2 films grown with and without PDA (**Supplementary Figure 9**). **Figure 7a** provides a highlighted top view of an FET with representative channel length (L_{Ch}) of 200nm device used for this study. We measured transfer characteristics of 100 such back-gated FETs fabricated from MoS_2 synthesized with and without a PDA step (**Figures 7b–c).** All 100 devices exhibit clean and uniform n-type transport behaviour within the applied bias range.

FETs devices made from MoS_2 films that underwent the PDA step have a room temperature median field effect mobility (μ_{FE}) of 25.4 $cm^2/V{\cdot}s$, with some devices exceeding 40 $cm^2/V{\cdot}s$. These devices feature high drain currents (I_{DS}) with a median I_{DS} = 209.9 µA/µm, and peak ($I_{DS\text{-}max}$) of 415.1 µA/µm. In comparison, FET devices that did not undergo the PDA step had lower median μ_{FE} = 15.6 $cm^2/V{\cdot}s$, which resulted in lower median I_{DS} = 125.7 µA/µm. Considering median and peak values, the MoS_2 channel whose synthesis incorporated the PDA process registered enhanced mobility and max drain current over the devices with non-PDA treated MoS_2 channels. These enhancements in μ_{FE} and I_{DS} in the

PDA-treated films can be correlated with the elimination of high-angle grain boundaries, the lower point defect-density and overall the superior crystalline quality of the MoS_2. The on/off current ratio (I_{on}/I_{off}) is ~10^8 for these MoS_2 FET devices, regardless of PDA treatment, with high performing examples exceeding 10^{10} owing to high drain-currents and strong gate-electrostatic control. **Figure 7d** compares median and peak values of I_{DS}, I_{on}/I_{off}, μ_{FE}, and subthreshold swing (*SS*) for 100 MoS_2 FETs with channels grown with and without PDA treatment. In addition to the PDA-related improvements in the electrical characteristics discussed above, the clear improvement in subthreshold swing (SS) can be attributed to reduced defects near the interface in the MoS_2 channel due to PDA anneal. We also note that the lower degree of threshold voltage (V_{TH}) variation in the MoS_2 channel grown with the PDA treatment signifies the uniformity of the crystal orientation and MoS_2 layer thickness. These FET device transfer characteristics reinforce the conclusion of a clear quality gap between the MoS_2 grown with and without a PDA step during MOCVD.

The resulting FET device performance is comparable to reports of monolayer MoS_2 transistors synthesized via scalable vapor-phase growth methods. Due to the convolution of device fabrication methods with the MOCVD growth technique, (precursor chemistries, reactor geometry, substrate selection and preparation etc.) and the impact on ultimate device performance, benchmarking of transistor metrics can be a challenge. We chose to delineate data from comparable references by the capacity for multi-wafer growth regardless of nuances of the MOCVD process or transistor fabrication. We did however choose to omit some well cited works that employ methods of complex sapphire substrate preparation, contact engineering, or incompatible growth methods beyond the scope of this work[75–77]. Benchmarks of carrier mobility and I_{on}/I_{off} are presented in **Figure 7e/f**[19,25,35,56,76,78]. Further details related to benchmarked references is available in **Supplementary Table 1**.

2.6 Additional TMDs

As seen in the optical image of **Figure 1c,** our process translates to multi-wafer growth of WS_2, WSe_2, and $MoSe_2$. **Supplementary Figure 10** provides supplemental characterization and device results for these additional TMD layers using the cooperative reconstructive epitaxial approach developed in this study. In each case, the use of a PDA post-MOCVD growth produces double-stepped sapphire surfaces covered with a single-domain, low-defect density TMD film with high crystalline quality. We measure strong PL signatures at the characteristic photon energy for each of these TMD materials, and their primary Raman mode peak spacings are as expected for monolayers of each respective material[79–86]. We note that for the selenide TMDs there are Raman peaks present that are consistent with bilayer modes, which indicates that some overgrowth is occurring in these as-yet unoptimized processes.

3. Materials and Methods

3.1 TMD Deposition

The TMD wafers produced in this study were deposited in an AIXTRON close-coupled showerhead (CCS) MOCVD system, equipped with an Argus topside temperature control (TTC) unit as well as a Laytec EpiTT, a schematic of which is depicted in **Figure 1**. This MOCVD platform has demonstrated scalability on sapphire in industry relevant wafer diameters[87]. Reactor temperature setpoints are controlled through the TTC and monitored by the Laytec EpiTT True Temperature reading. Rather than growing to time, all TMD processes are grown to an endpoint determined by an in-situ 405 nm photoreflectance (PR) measurement that corresponds to a coalesced monolayer[88]. Precursors for TMD growth are molybdenum/tungsten hexacarbonyl ($M(CO)_6$ used from here forward to refer to transition metal carbonyl) and hydrogen sulphide/selenide (H_2S/H_2Se). A multistate recipe was designed to be a basis of optimization for the TMD family of materials, focusing first on MoS_2. Substrates used in this study are non-prime grade c-plane sapphire 50.8 mm diameter wafers with 0.2° ± 0.1° off-cut towards the m-plane purchased from University Wafer.

A multistage growth process carefully controls precursor flow and reactor conditions starting with sapphire pretreatment, TMD deposition, and ending with a post deposition anneal (PDA) of the monolayer. The process begins with a 1000° C anneal in H_2 ambient for 15 minutes to clean the sapphire surface and initiate terrace reconstruction. At 15 minutes, a dilute flow 89 µmol/min (2 sccm) of H_2S is sent to the reactor to enhance smoothing of the terrace edge roughness and passivate the sapphire surface. Upon completion of the pretreatment, H_2S flow is stopped, and reactor temperature is rapidly reduced to 700° C and held for 5 minutes, with the intent of quenching further uncontrolled modification of the sapphire surface[46]. After the 5-minute hold at 700° C, the carrier gas is switched from H_2 to N_2 and the reactor ramps to the nucleation temperature and pressure of 800° C and 50 mbar respectively. Once the nucleation temperature is stable across the susceptor the EpiTT conducts a substrate specific calibration, and the PR value is set to a respective value. A constant H_2S flow of 707 µmol/min starts and the $M(CO)_6$ bubbler opens at 10 nmol/min and is ramped to 18 nmol/min over the course of 5 minutes. Nucleation continues for a further 5 minutes with the $M(CO)_6$ flow held at this higher rate, for a total of 10 minutes. The PR reading climbs during this step as material is deposited on the surface, depicted in **Supplementary Figure 3**. $M(CO)_6$ flow is then directed to the vent and the reactor ramps to growth conditions, 850° C and 15 mbar while the H_2S flow is maintained to the reactor. Upon reaching growth conditions a period of 15 minutes serves as a stabilization step as well as an opportunity for ripening of the TMD islands formed in the previous low-temperature nucleation step.[89]. The $M(CO)_6$ is then redirected to the reactor to continue growth of the TMD monolayer at the same 18 nmol/min. The PR signal, which remains constant when no $M(CO)_6$ is being injected into the chamber, begins climbing

again. Once the PR signal reaches a total change of 1.7% from its starting value, the $M(CO)_6$ bubbler conditions are modulated to taper precursor flow from 18 nmol/min towards 7 nmol/min to mitigate bilayer growth[90]. This tapering is visible in the PR signal as the process continues to its endpoint of 2.7% total reflectance change. At the desired endpoint, $M(CO)_6$ flow to the reactor is stopped and the reactor ramps to the PDA conditions of 1000 °C and 150 mbar while the H_2S flow continues unchanged. The PDA lasts for 30 minutes and once complete, the reactor begins cooling in N_2/H_2S. H_2S flow continues during cooldown until 300 °C. Once the reactor reaches 150 °C cycle purging is conducted and the wafers can be removed.

For WS_2, the process was the same as for MoS_2 apart from addressing the $W(CO)_6$ bubbler. For the selenide processes, during the limited initial attempts, a decreasing trendline in the photoreflectance signal indicated possible etching due to overly high temperatures. For $MoSe_2$ and WSe_2, the modular base recipe was modified to reduce the PDA temperature to 850ºC and 800 °C respectively. The growth temperature of the WSe_2 process was also reduced to 800 °C making it a constant temperature process. The reactor pressure parameters were also adjusted to 300 mbar for nucleation and growth and 500 mbar for the PDA. No further optimization of these materials was attempted in this study but will be the subject of future work. It is important to note that the sapphire pretreatment prior to selenide based TMD deposition was still conducted using H_2S, switching to H_2Se for nucleation, growth, and PDA stages. No studies into H_2Se-based sapphire treatments were performed during this work.

3.2 Material Characterization

3.2.1 Spectroscopic Techniques

Raman and photoluminescence (PL) spectroscopy was conducted using a Horiba LabRAM HR Evolution confocal scanning Raman microscope. For Raman a 532 nm laser and for PL a 441 nm laser was used in conjunction with a 100× objective, 100 mm aperture, 1800/600 grooves per mm grating, and 5%/1% neutral density (ND) filters respectively.

XPS data was collected at room temperature, illuminating the sample with photons from a Specs XR50 source at 300 W, using a non-monochromatized Al Kα anode, having the main line at 1486.61 eV. The electrons were filtered in energy using a Specs Astraios 190 electron analyzer and the signal was recorded onto a Specs 2D-CMOS detector. The spectra were fitted by first subtracting a Tougaard-type background before using symmetric Voigt doublets as lineshape for the S 2p core level spectra.

ARPES data was collected at room temperature, using photons generated from a Specs micro-Sirius UV lamp and using a grating to select HeI line at 21.2 eV. The UV light was focused onto the sample at 70 μm using a metal-coated capillary. The electrons were collected, filtered in energy using a

Specs Astraios 190 electron analyzer and dispersed onto a Specs 2D-CMOS detector. The bands were extracted from 3D scans carried out using electrostatic lens deflectors. The curvature plot was created following the procedure described by P. Zhang et. al[74].

3.2.2 Diffractive Techniques

In plane XRD measurements were conducted on a PAnalytical X'pert3MRD. LEED data was recorded at room temperature using a Specs ErLEED 150 instrument acquired at a primary beam energy of 95 eV. The RHEED measurements used a high-energy electron beam operated at an accelerating voltage of 14 kV in another chamber with ultra-high vacuum at the base pressure of 10^{-9} to 10^{-10} Torr. The electron beam was incident on the sample surface at a grazing angle. Diffraction patterns were collected along multiple in-plane azimuthal directions by rotating the sample about its surface normal. The beam was aligned along the major flat of the samples and resulting diffraction pattern recorded using a phosphor screen coupled to a digital camera system. We analyzed the obtained diffraction patterns to determine surface symmetry, reconstruction, and crystallographic orientation. We used the spacing between diffraction features in reciprocal space to calculate in-plane real space lattice constants.

3.2.3 Microscopy

Atomic force microscopy (AFM) was conducted on a Bruker Dimension Icon. For annealed sapphire and nucleation, a scanasyst-air probe was used in Peak Force tapping mode. Once there is significant TMD coverage, an attractive force from the surface makes data acquisition challenging and scanning in Peak Force quantitative nanomechanical mapping with a Scout 350 RAI probe is used. This stiffer probe can image with a sufficiently low Peak Force amplitude while resisting electrostatic interactions with the surface.

C-AFM images were collected using a Dimension Icon AFM instrument in PF-TUNA mode. Measurements were performed over 5500×500 nm^2 areas, with higher-resolution scans conducted on 200×200 nm^2 and 75×75 nm^2 regions. A direct current (DC) voltage bias was applied to the electrically connected sample. During data acquisition, the conductive probe connected to the current detector served as a virtual ground.

A cross-sectional lamella for STEM imaging was prepared using a ThermoFisher Scios 2 dual beam focused ion beam – scanning electron microscope (FIB-SEM). Initial trenching was performed using a 30 kV gallium ion beam. A final polishing step at 2 kV gallium ion beam was used to remove residual surface damage and achieve electron transparency for STEM imaging.

Cross-sectional atomic-resolution STEM imaging was performed using a double spherical-aberration-corrected FEI Titan 3 G2 operated at 300 kV with a probe current of 100 pA. HAADF-STEM

images were acquired using a camera length of 115 mm, corresponding to a collection angle of 42-244 mrad, with a probe convergence semi-angle of 30 mrad. STEM- energy dispersive X-ray spectroscopy (EDS) was performed using a Super-X EDS detector and elemental mappings were generated using Bruker ESPRIT software. Raw HAADF-STEM images were filtered using a Fast Fourier Transform bandpass filter applied in ImageJ to improve image contrast. Image intensity line scans were performed using Gatan Digtal Micrograph software.

Imaging spectroscopic ellipsometry (ISE) measurements were performed using an EP4 system (Park Systems GmbH, Germany) operating over a spectral range of 400–700 nm with a spectral bandwidth of approximately 4 nm. Measurements were acquired at angles of incidence of 50° and 55°. The instrument employs a polarizer–compensator–sample–analyzer (PCSA) optical configuration, in which a charge-coupled device (CCD) camera coupled with a magnification objective serves as the detector, enabling a lateral spatial resolution of approximately 1 μm. The ellipsometric angles Δ and Ψ were extracted from the complex reflectance ratio defined as:

$$\tilde{\rho} = \frac{\tilde{r}_p}{\tilde{r}_s} = \tan(\Psi)\, e^{i\Delta}$$

where $\tilde{r}_p$ and $\tilde{r}_s$ denote the complex reflection coefficients for the parallel (p) and orthogonal (s) polarization components, respectively.

The experimental ISE data acquired from the MoS_2 TMD monolayer was analyzed using an optical multilayer model. The multilayer stack was constructed as air / TMD / Al_2O_3 and the layer thicknesses and dielectric functions were determined through regression analysis. The dielectric function of the Al_2O_3 substrate was characterized independently prior to the fitting procedure in order to reduce the number of free parameters. The dielectric response of the TMD monolayer was modeled as a sum of four Tauc–Lorentz oscillators to capture both excitonic and interband optical transitions. Thickness values averaged over five spatially separated measurement locations yielded 0.62 ± 0.01 nm, consistent with monolayer MoS_2 character.

For wafer-scale uniformity assessment across a 2-inch substrate, a 5× objective was employed, yielding a field of view of 1250 × 850 μm. Spatial sampling was performed by binning 3 × 3 pixels, resulting in an effective lateral resolution of approximately 12 μm. ISE mapping revealed that the TMD monolayer was grown with high spatial uniformity, exhibiting a thickness variation of less than ~3% relative to the mean value across the wafer surface.

3.4 Device Fabrication and Electrical Characterization

A p++ Si wafer with 285nm SiO_2 thermally grown oxide was treated in buffered-oxide-etchant (BOE) 1:7 for 15 minutes and then cleaned with de-ionized (D.I.) water followed by deposition of 5nm Ti and 20nm Pt by electron-beam evaporation to serve as the back gate electrodes. Next 25nm Al_2O_3 was grown by atomic layer deposition (ALD) on Pt using the Kurt. J. Lesker 150 LE ALD tool.

Monolayer MoS_2 and other TMD layers were wet-transferred from our as-grown TMD-on-sapphire MOCVD samples described above onto 25 nm Al_2O_3 back-gate dielectric stacks. The transfer process is described in our previous works[91–94]. The substrate surface was coated with PMMA A6 by spin-coating at 4000 rpm for 45 s and then baked at 180 °C for 90 s. Pattern definition was carried out using a Raith EBPG5200 electron-beam lithography system, after which the resist was developed for 60 s in a 1:1 mixture of methyl iso-butyl ketone (MIBK) and iso-propyl alcohol (IPA), followed by a 45 s rinse in IPA. The patterned TMD regions were subsequently etched using an SF_6-based RIE process performed at 5 °C for 11s. The remaining e-beam resist was removed by sequential dissolution in acetone and IPA.

A second lithography step was then performed to define the source and drain electrodes. The substrate was spin-coated at 4000 rpm for 45 s, this time with a bilayer of MMA EL6 and PMMA A3, which were baked at 150 °C and 180 °C for 90 s each. Electron-beam lithography was repeated to expose the electrode patterns, and the resist was developed in MIBK/IPA followed by an IPA rinse, similar to the first step. To form the metal contacts, we deposited 15nm Ni followed by a 45 nm Au layer using e-beam evaporation. Finally, excess Ni/Au was removed through a liftoff process by soaking the sample in acetone for 45 min followed by gentle agitation and then rinsing it in IPA for 10 min to clean the surface.

Electrical characterization was performed in ambient conditions using a Formfactor 12000 semi-automatic probe station integrated with a Keysight B1500A semiconductor parameter analyzer. FET transfer curves were collected by measuring the drain current (I_{DS}) variation on sweeping the back-gate bias (V_{BG}) from -6 V to 6 V at a constant drain bias (V_{DS}) of $1V$.

Conclusion

This work demonstrates an industry-relevant route for the deposition of wafer-scale single-crystal, single-domain TMD monolayers by leveraging a cooperative reconstructive epitaxy mechanism on c-plane sapphire. By integrating controlled sapphire pretreatment, in-situ photoreflectance endpoint detection, and a high-temperature hydride post-deposition anneal within a single continuous process, we simultaneously achieve substrate double-step formation, domain alignment, sulfur vacancy passivation and grain boundary annihilation. The observation that sapphire step evolution differs in the presence of the growing TMD layer supports a coupled reconstruction mechanism between substrate and overlayer, that differs from individual thermal reconstruction pathways for the substrate and monolayer. Structural,

spectroscopic, and electronic measurements collectively confirm the formation of a high quality, epitaxially registered 2H-MoS_2 monolayer. We anticipate that it will be possible to systematically translate this modular process from MoS_2 to other members of the TMD family. The utilization of standard on-axis cut c-plane sapphire leverages an existing, mature substrate supply chain and avoids reliance on specialized miscut or engineered surfaces, supporting a more economically scalable pathway for manufacturing. These results help drive the maturation of TMD synthesis by MOCVD, supporting efforts to make this family of materials commercially viable in next generation technologies.

Author contributions

D.E. and M.C. conceived of the experiments. T.V. transferred materials for TEM analysis. S.D., M.D., and K.M. fabricated test structures and conducted electrical testing. P.S. and M.B. conducted RHEED analysis. C.C., S.F., and A.R. conducted XPS, ARPES, and LEED analysis. D.N., D.S. processed and imaged samples by TEM under the supervision of M.T. J.R. and L.L. conducted in-plane XRD analysis. M.D. and A.R. collected ISE data. N.G., L.T., and K.E. conducted GIXRD analysis. S.K., C.M., and A.H. provided support on MOCVD process development. All authors provided input on manuscript.

Data availability

Conflicts of interest

The authors declare no competing financial interests.

Funding Statement

This material is based upon work supported under a University Nuclear Leadership Program Graduate Fellowship. The authors acknowledge infrastructure support from the Department of Energy Nuclear Science User Facilities General Infrastructure Program through award numbers DE-NE0008677 and DE-NE0008496. Additionally, we acknowledge infrastructure support from the Idaho Workforce Development Council. Any opinions, findings, conclusions or recommendations expressed in this publication are those of the author(s) and do not necessarily reflect the views of the Department of Energy Office of Nuclear Energy. This work was supported in part by the Air Force Research Laboratory (AFRL) under Agreement Number FA8650-20-2-5506. The U.S. Government is authorized to reproduce and distribute reprints for Governmental Purposes notwithstanding any copyright notation thereon. M.T. and D.S. acknowledge the Pennsylvania State University Materials Characterization Lab Core Facility, Materials Research Institute, University Park, PA (PRID:SCR_012386) for use of Scios 2 and Titan 3 G2

and Wesley Auker and Ke Wang for their help with cross-sectional lamella sample preparation and HAADF-STEM imaging.

References

1. Ha, V.-A. & Giustino, F. High-throughput screening of 2D materials identifies p-type monolayer WS2 as potential ultra-high mobility semiconductor. *NPJ Comput. Mater.* **10**, 229 (2024).

2. Mak, K. F., Lee, C., Hone, J., Shan, J. & Heinz, T. F. Atomically Thin MoS2: A New Direct-Gap Semiconductor. *Phys. Rev. Lett.* **105**, 136805 (2010).

3. Splendiani, A. *et al.* Emerging Photoluminescence in Monolayer MoS2. *Nano Lett.* **10**, 1271–1275 (2010).

4. O'Brien, K. P. *et al.* Process integration and future outlook of 2D transistors. *Nat. Commun.* **14**, 6400 (2023).

5. IRDS: International Roadmap for Devices and Systems. *IRDS 2024 edition* Preprint at (2024).

6. Nicolosi, V., Chhowalla, M., Kanatzidis, M. G., Strano, M. S. & Coleman, J. N. Liquid Exfoliation of Layered Materials. *Science (1979).* **340**, 1226419 (2013).

7. Coleman, J. N. *et al.* Two-Dimensional Nanosheets Produced by Liquid Exfoliation of Layered Materials. *Science (1979).* **331**, 568–571 (2011).

8. Zheng, J. *et al.* High yield exfoliation of two-dimensional chalcogenides using sodium naphthalenide. *Nat. Commun.* **5**, 2995 (2014).

9. Zhou, K.-G., Mao, N.-N., Wang, H.-X., Peng, Y. & Zhang, H.-L. A Mixed-Solvent Strategy for Efficient Exfoliation of Inorganic Graphene Analogues. *Angew. Chem. Int. Ed.* **50**, 10839–10842 (2011).

10. Smith, R. J. *et al.* Large-Scale Exfoliation of Inorganic Layered Compounds in Aqueous Surfactant Solutions. *Advanced Materials* **23**, 3944–3948 (2011).

11. Liu, K.-K. *et al.* Growth of Large-Area and Highly Crystalline MoS2 Thin Layers on Insulating Substrates. *Nano Lett.* **12**, 1538–1544 (2012).

12. Shi, Y. *et al.* van der Waals Epitaxy of MoS2 Layers Using Graphene As Growth Templates. *Nano Lett.* **12**, 2784–2791 (2012).

13. Lin, Y.-C. *et al.* Wafer-scale MoS2 thin layers prepared by MoO3 sulfurization. *Nanoscale* **4**, 6637–6641 (2012).

14. Novoselov, K. S. *et al.* Electric Field Effect in Atomically Thin Carbon Films. *Science (1979).* **306**, 666–669 (2004).

15. Novoselov, K. S. *et al.* Two-dimensional atomic crystals. *Proceedings of the National Academy of Sciences* **102**, 10451–10453 (2005).

16. Radisavljevic, B., Radenovic, A., Brivio, J., Giacometti, V. & Kis, A. Single-layer MoS2 transistors. *Nat. Nanotechnol.* **6**, 147–150 (2011).

17. Eichfeld, S. M. *et al.* Highly Scalable, Atomically Thin WSe2 Grown via Metal–Organic Chemical Vapor Deposition. *ACS Nano* **9**, 2080–2087 (2015).

18. Ishihara, S. *et al.* MOCVD of Monolayer MoS2 using Novel Molybdenum Precursor i-Pr2DADMo(CO)3. *MRS Adv.* **3**, 379–384 (2018).

19. Cun, H. *et al.* Wafer-scale MOCVD growth of monolayer MoS2 on sapphire and SiO2. *Nano Res.* **12**, 2646–2652 (2019).

20. Gong, Y., Zhang, X., Redwing, J. M. & Jackson, T. N. Thin Film Transistors Using Wafer-Scale Low-Temperature MOCVD WSe2. *J. Electron. Mater.* **45**, 6280–6284 (2016).

21. Liu, M. *et al.* Periodical Ripening for MOCVD Growth of Large 2D Transition Metal Dichalcogenide Domains. *Adv. Funct. Mater.* **33**, 2212773 (2023).

22. Kim, T. S. *et al.* Gas-Phase Alkali Metal-Assisted MOCVD Growth of 2D Transition Metal Dichalcogenides for Large-Scale Precise Nucleation Control. *Small* **18**, 1–9 (2022).

23. Mc Knight, T. V, Choudhury, T. H., Wang, K., Bansal, A. & Redwing, J. M. MOCVD Growth of Tungsten Ditelluride Thin Films. *J. Cryst. Growth* **625**, 127436 (2024).

24. Tang, H. *et al.* Nucleation and coalescence of tungsten disulfide layers grown by metalorganic chemical vapor deposition. *J. Cryst. Growth* **608**, 127111 (2023).

25. Choudhury, T. H. *et al.* Comparison of the MOCVD growth and properties of wafer-scale transition metal dichalcogenide epitaxial monolayers. *2d Mater.* **12**, 045009 (2025).

26. Marx, M. *et al.* Large-area MoS2 deposition via MOVPE. *J. Cryst. Growth* **464**, 100–104 (2017).

27. T. H. Choudhury, M. Chubarov & J. M. Redwing. Large area epitaxial 2D transition metal dichalcogenide films grown by gas source chemical vapor deposition.

28. Chen, X. *et al.* Orientation domain dispersions in wafer scale epitaxial monolayer WSe2 on sapphire. *Appl. Surf. Sci.* **567**, 150798 (2021).

29. Chubarov, M. *et al.* Wafer-Scale Epitaxial Growth of Unidirectional WS2 Monolayers on Sapphire. *ACS Nano* **15**, 2532–2541 (2021).

30. Zhu, H. *et al.* Step engineering for nucleation and domain orientation control in WSe2 epitaxy on c-plane sapphire. *Nat. Nanotechnol.* **18**, 1295–1302 (2023).

31. Lin, Y.-C. *et al.* Realizing Large-Scale, Electronic-Grade Two-Dimensional Semiconductors. *ACS Nano* **12**, 965–975 (2018).

32. Liu, L. *et al.* Uniform nucleation and epitaxy of bilayer molybdenum disulfide on sapphire. *Nature* **605**, 69–75 (2022).

33. Li, C. *et al.* Revisiting the Epitaxial Growth Mechanism of 2D TMDC Single Crystals. *Advanced Materials* **36**, 2404923 (2024).

34. Li, T. *et al.* Epitaxial growth of wafer-scale molybdenum disulfide semiconductor single crystals on sapphire. *Nat. Nanotechnol.* **16**, 1201–1207 (2021).

35. Shi, Y. *et al.* Engineering Wafer-Scale Epitaxial Two-Dimensional Materials through Sapphire Template Screening for Advanced High-Performance Nanoelectronics. *ACS Nano* **15**, 9482–9494 (2021).

36. Mo, J. *et al.* Importance of the substrate's surface evolution during the MOVPE growth of 2D-transition metal dichalcogenides. *Nanotechnology* **31**, (2020).

37. Ji, R. *et al.* Step-edge controlled fast growth of wafer-scale MoSe2 films by MOCVD. *Nano Res.* **16**, 9577–9583 (2023).

38. Zhang, Z., Yang, X., Liu, K. & Wang, R. Epitaxy of 2D Materials toward Single Crystals. *Advanced Science* **9**, 2105201 (2022).

39. Yang, P. *et al.* Epitaxial growth of inch-scale single-crystal transition metal dichalcogenides through the patching of unidirectionally orientated ribbons. *Nat. Commun.* **13**, 3238 (2022).

40. Wang, J. *et al.* Dual-coupling-guided epitaxial growth of wafer-scale single-crystal WS2 monolayer on vicinal a-plane sapphire. *Nat. Nanotechnol.* **17**, 33–38 (2022).

41. Dumcenco, D. *et al.* Large-Area Epitaxial Monolayer MoS2. *ACS Nano* **9**, 4611–4620 (2015).

42. Fu, J.-H. *et al.* Oriented lateral growth of two-dimensional materials on c-plane sapphire. *Nat. Nanotechnol.* **18**, 1289–1294 (2023).

43. Kandybka, I. *et al.* Chemical Vapor Deposition of a Single-Crystalline MoS2 Monolayer through Anisotropic 2D Crystal Growth on Stepped Sapphire Surface. *ACS Nano* **18**, 3173–3186 (2024).

44. Huang, L.-Y. *et al.* Wafer-Scale Single-Crystal WSe2 Monolayers Using Substrate-Passivation-Driven Epitaxy. *ACS Nano* **20**, 2104–2113 (2026).

45. Curiotto, S. & Chatain, D. Surface morphology and composition of c-, a- and m-sapphire surfaces in O2 and H2 environments. *Surf. Sci.* **603**, 2688–2697 (2009).

46. Yatsui, T., Kuribara, K., Sekitani, T., Someya, T. & Yoshimoto, M. Temperature-modulated annealing of c-plane sapphire for long-range-ordered atomic steps. *J. Phys. D Appl. Phys.* **49**, 115302 (2016).

47. Yoshimoto, M. *et al.* Atomic-scale formation of ultrasmooth surfaces on sapphire substrates for high-quality thin-film fabrication. *Appl. Phys. Lett.* **67**, 2615–2617 (1995).

48. Wang, R., Guo, D., Xie, G. & Pan, G. Atomic Step Formation on Sapphire Surface in Ultra-precision Manufacturing. *Sci. Rep.* **6**, 29964 (2016).

49. Torsi, R. *et al.* Impact of Sapphire Substrate Reconstruction on the Structural, Electronic, and Photonic Properties of MoS2. *Small* **n/a**, e11179 (2026).

50. Nakamura, S. & Krames, M. R. History of Gallium–Nitride-Based Light-Emitting Diodes for Illumination. *Proceedings of the IEEE* **101**, 2211–2220 (2013).

51. Akselrod, M. S. & Bruni, F. J. Modern trends in crystal growth and new applications of sapphire. *J. Cryst. Growth* **360**, 134–145 (2012).

52. Chiang, Y., Birnie, D. P. . & Kingery, W. D. . *Physical Ceramics*. (Wiley, 1997).

53. Refinement of the α Al2O3, Ti2O3, V2O3 and Cr2O3 structures*. **117**, 235–237 (1962).

54. Yu, H. *et al.* Wafer-Scale Growth and Transfer of Highly-Oriented Monolayer MoS2 Continuous Films. *ACS Nano* **11**, 12001–12007 (2017).

55. Toofan, J. & Watson, P. R. The termination of the α-Al2O3 (0001) surface: a LEED crystallography determination. *Surf. Sci.* **401**, 162–172 (1998).

56. Sakuma, Y. *et al.* Self-aligned and self-limiting van der Waals epitaxy of monolayer MoS2 for scalable 2D electronics. *Nat. Commun.* **17**, 602 (2026).

57. Godin, K., Cupo, C. & Yang, E.-H. Reduction in Step Height Variation and Correcting Contrast Inversion in Dynamic AFM of WS2 Monolayers. *Sci. Rep.* **7**, 17798 (2017).

58. Xiang, Y. *et al.* Monolayer MoS2 on sapphire: an azimuthal reflection high-energy electron diffraction perspective. *2d Mater.* **8**, 025003 (2021).

59. Pham Van, L., Kurnosikov, O. & Cousty, J. Evolution of steps on vicinal (0001) surfaces of α-alumina. *Surf. Sci.* **411**, 263–271 (1998).

60. Mortelmans, W. *et al.* Peculiar alignment and strain of 2D WSe2 grown by van der Waals epitaxy on reconstructed sapphire surfaces. *Nanotechnology* **30**, 465601 (2019).

61. Lauritsen, J. V *et al.* Atomic-Scale Structure and Stability of the √(31) x √(31) R9 Surface of Al2O3 (0001). *Phys. Rev. Lett.* **103**, 76103 (2009).

62. Curtis, M. *et al.* Assessment of wafer scale MoS2 atomic layers grown by metal–organic chemical vapor deposition using organo-metal, organo-sulfide, and H2S precursors. *RSC Adv.* **14**, 22618–22626 (2024).

63. Dickinson, R. G. & Pauling, L. The Crystal Structure of Molybdenite. *J. Am. Chem. Soc.* **45**, 1466–1471 (1923).

64. Gołasa, K. *et al.* Resonant Raman Scattering in MoS2- From Bulk to Monolayer. *Solid State Commun.* **197**, 53–56 (2014).

65. Andrzejewski, D. *et al.* Improved luminescence properties of MoS2 monolayers grown via MOCVD: Role of pre-treatment and growth parameters. *Nanotechnology* **29**, (2018).

66. Lee, C. *et al.* Anomalous lattice vibrations of single- and few-layer MoS2. *ACS Nano* **4**, 2695–2700 (2010).

67. Li, H. *et al.* From Bulk to Monolayer MoS2: Evolution of Raman Scattering. *Adv. Funct. Mater.* **22**, 1385–1390 (2012).

68. Gontijo, R. N. *et al.* Multiple excitations and temperature study of the disorder-induced Raman bands in MoS2. *2d Mater.* **8**, 035042 (2021).

69. Mak, K. F. *et al.* Tightly Bound Trions in Monolayer MoS2. *Nat. Mater.* **12**, 207–211 (2013).

70. Park, J.-H. *et al.* Synthesis of High-Performance Monolayer Molybdenum Disulfide at Low Temperature. *Small Methods* **5**, (2021).

71. Ghiami, A. *et al.* Impact of Carbon Impurities on Air Stability of MOCVD 2D-MoS2. *Surfaces* **6**, 351–363 (2023).

72. Martincová, J., Otyepka, M. & Lazar, P. Is Single Layer MoS2 Stable in the Air? *Chemistry - A European Journal* **23**, 13233–13239 (2017).

73. Leonhardt, A. *et al.* Improving MOCVD MoS2 Electrical Performance: Impact of Minimized Water and Air Exposure Conditions. *IEEE Electron Device Letters* **38**, 1606–1609 (2017).

74. Zhang, P. *et al.* A precise method for visualizing dispersive features in image plots. *Review of Scientific Instruments* **82**, 043712 (2011).

75. Zou, X. *et al.* Robust epitaxy of single-crystal transition-metal dichalcogenides on lanthanum-passivated sapphire. *Science (1979).* **390**, eaea0849 (2026).

76. Moon, G. *et al.* Single-crystalline monolayer semiconductors with coherent quantum transport by vicinal van der Waals epitaxy. *Nat. Electron.* **8**, 1182–1190 (2025).

77. Liu, L. *et al.* Kinetic acceleration of MoS2 growth by oxy-metal-organic chemical vapor deposition. *Science (1979).* **391**, 494–498 (2026).

78. Sebastian, A., Pendurthi, R., Choudhury, T. H., Redwing, J. M. & Das, S. Benchmarking monolayer MoS2 and WS2 field-effect transistors. *Nat. Commun.* **12**, 693 (2021).

79. del Corro, E. *et al.* Excited Excitonic States in 1L, 2L, 3L, and Bulk WSe2 Observed by Resonant Raman Spectroscopy. *ACS Nano* **8**, 9629–9635 (2014).

80. Nam, D., Lee, J.-U. & Cheong, H. Excitation energy dependent Raman spectrum of MoSe2. *Sci. Rep.* **5**, 17113 (2015).

81. Tonndorf, P. *et al.* Photoluminescence emission and Raman response of monolayer MoS2, MoSe2, and WSe2. *Opt. Express* **21**, 4908–4916 (2013).

82. Berkdemir, A. *et al.* Identification of individual and few layers of WS2 using Raman Spectroscopy. *Sci. Rep.* **3**, 1–8 (2013).

83. Peimyoo, N. *et al.* Thermal conductivity determination of suspended mono- and bilayer WS2 by Raman spectroscopy. *Nano Res.* **8**, 1210–1221 (2015).

84. Kim, K., Lee, J. U., Nam, D. & Cheong, H. Davydov Splitting and Excitonic Resonance Effects in Raman Spectra of Few-Layer MoSe2. *ACS Nano* **10**, 8113–8120 (2016).

85. Shi, W. *et al.* Raman and photoluminescence spectra of two-dimensional nanocrystallites of monolayer WS2 and WSe2. *2d Mater.* **3**, (2016).

86. Del Corro, E. *et al.* Atypical Exciton-Phonon Interactions in WS2 and WSe2 Monolayers Revealed by Resonance Raman Spectroscopy. *Nano Lett.* **16**, 2363–2368 (2016).

87. Schram, T. *et al.* Integration and electrical evaluation of WS2 and MoS2 fets in a 300 mm pilot line. *Discover Electronics* **3**, 15 (2026).

88. Li, Y. *et al.* Measurement of the Optical Dielectric Function of Monolayer Transition-Metal Dichalcogenides: MoS2, MoSe2, WS2, and WSe2. *Phys. Rev. B* **90**, 205422 (2014).

89. Zhang, X. *et al.* Diffusion-Controlled Epitaxy of Large Area Coalesced WSe2 Monolayers on Sapphire. *Nano Lett.* **18**, 1049–1056 (2018).

90. Tang, S. *et al.* Migration-Enhanced Metal–Organic Chemical Vapor Deposition of Wafer-Scale Fully Coalesced WS2 and WSe2 Monolayers. *Cryst. Growth Des.* **23**, 1547–1558 (2023).

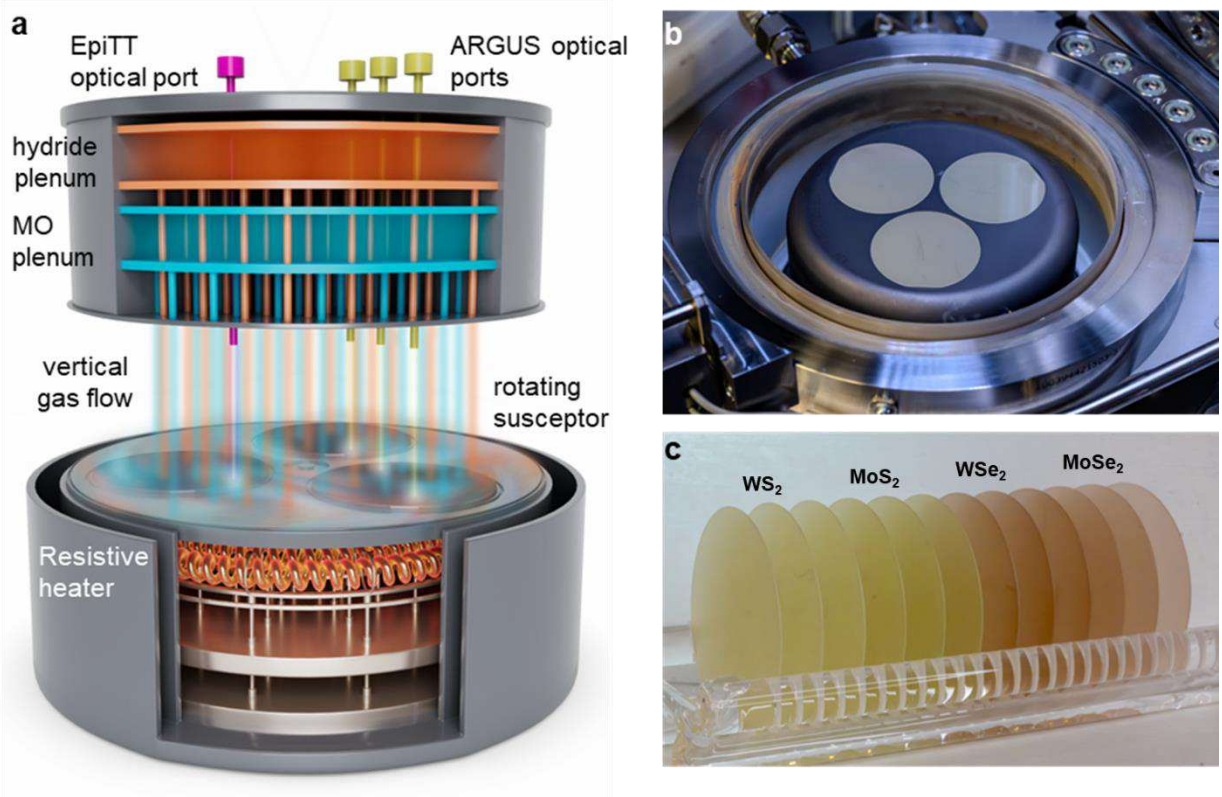
91. Sen, D. *et al.* Multifunctional 2D FETs exploiting incipient ferroelectricity in freestanding SrTiO3 nanomembranes at sub-ambient temperatures. *Nat. Commun.* **15**, 10739 (2024).

92. Rasyotra, A. *et al.* Nanosheets Derived from Titanium Diboride as Gate Insulators for Atomically Thin Transistors. *ACS Nano* **19**, 19646–19658 (2025).

93. Jayachandran, D. *et al.* Insect-Inspired, Spike-Based, in-Sensor, and Night-Time Collision Detector Based on Atomically Thin and Light-Sensitive Memtransistors. *ACS Nano* **17**, 1068–1080 (2023).

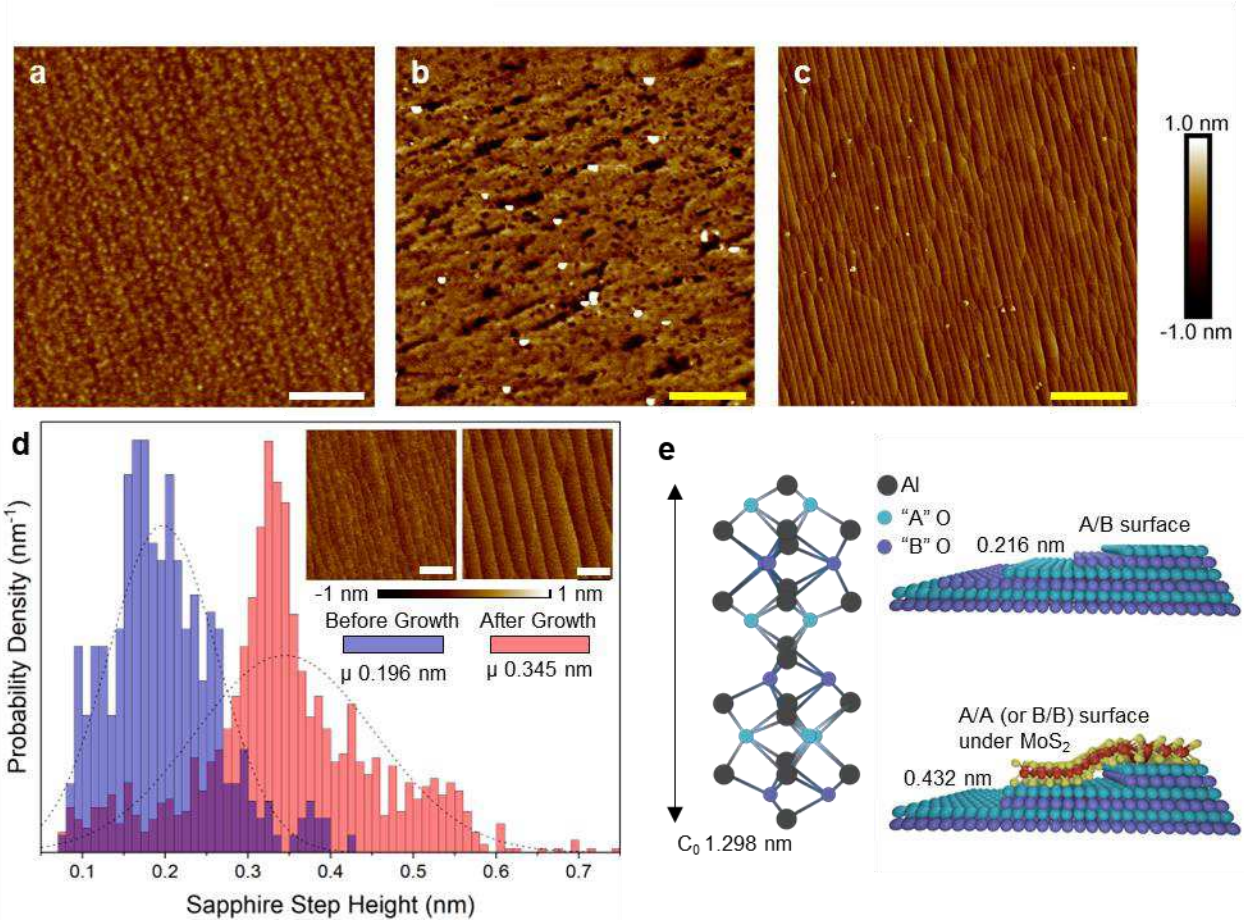
94. Subbulakshmi Radhakrishnan, S. *et al.* A Sparse and Spike-Timing-Based Adaptive Photoencoder for Augmenting Machine Vision for Spiking Neural Networks. *Advanced Materials* **34**, 2202535 (2022).

Figure 1



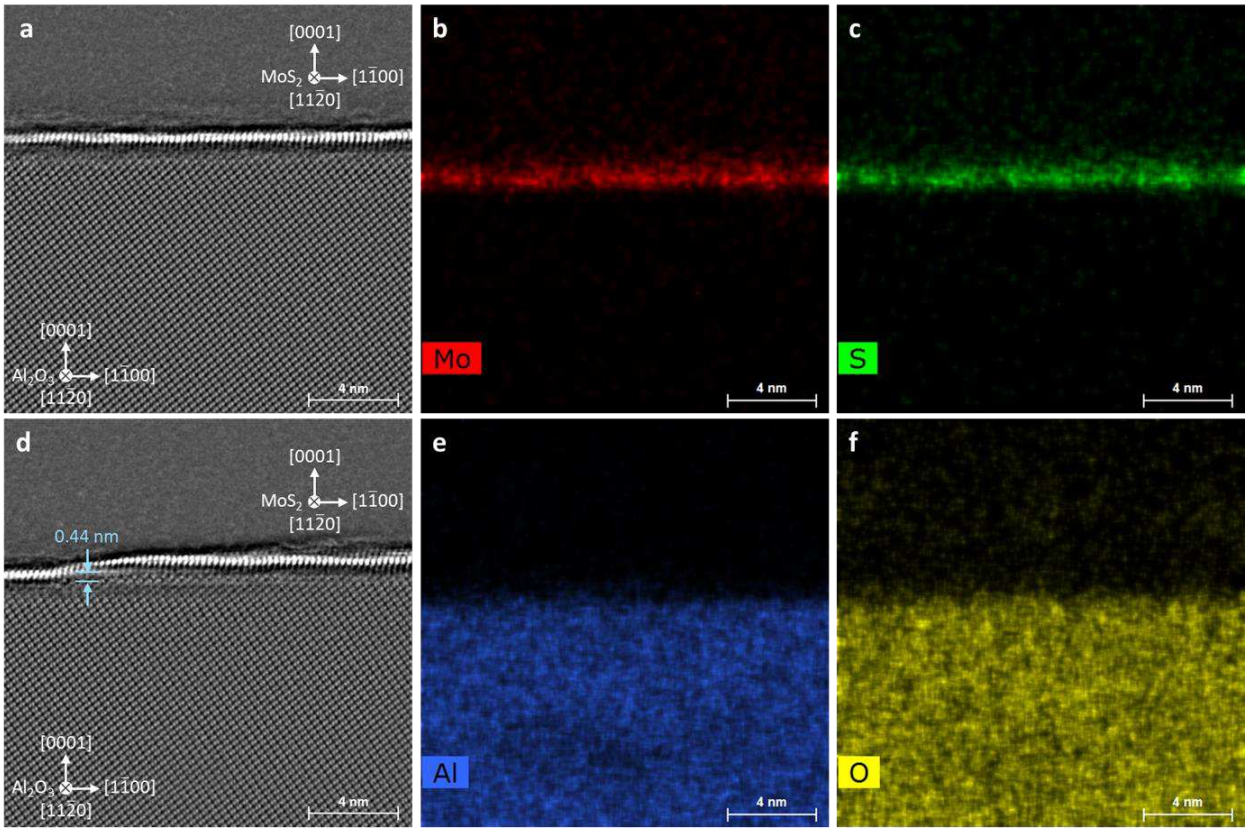
a, Schematic of close-coupled showerhead MOCVD reactor depicting dual precursor plenums and optical ports for in-situ instrumentation. **b**, Image of MoS_2 wafers in multi-wafer susceptor upon completion of growth process. **c**, Optical image of 50 mm wafers of all the TMDs grown as part of this study (Left to Right: MoS_2, WS_2, $MoSe_2$ and WSe_2).

Figure 2



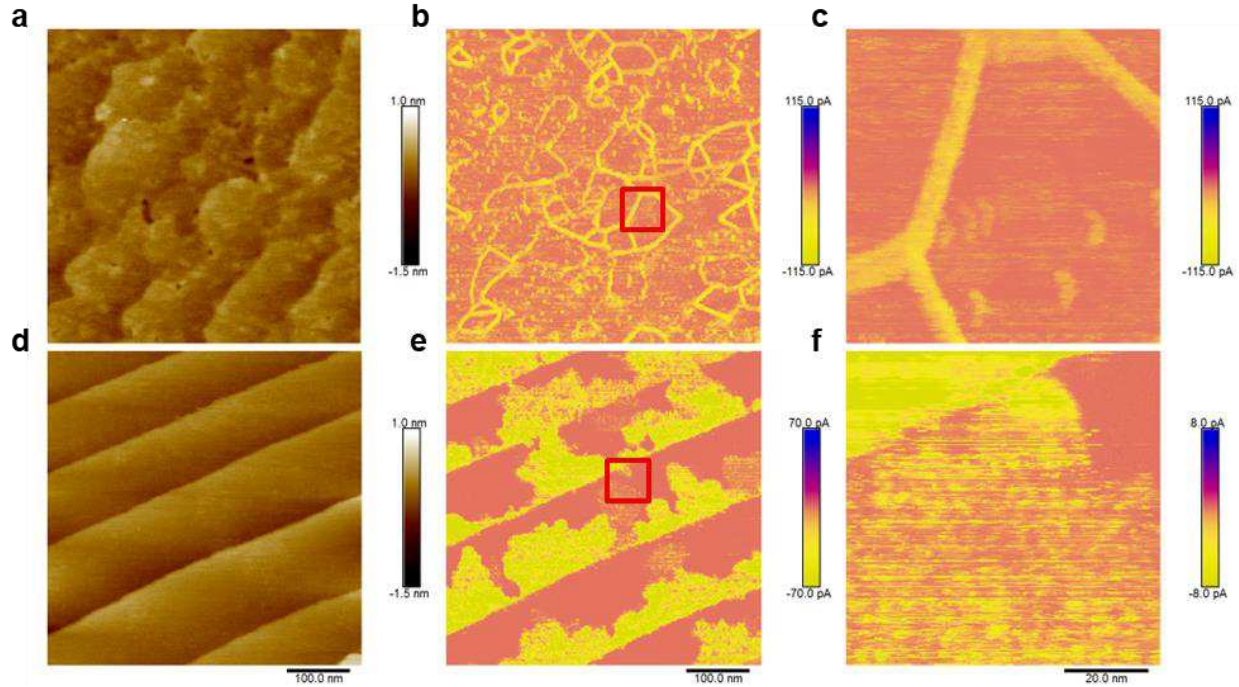
a, AFM topography of surface after MoS_2 nucleation. Nucleated domains of MoS_2 are small (<20 nm across) and dense across mono-stepped sapphire, with no indication of edge-guided nucleation that would precede step-flow growth. **b**, Monolayer MoS_2 surface at process endpoint as measured by in-situ photoreflectance appears very rough (Ra and Rq of 0.090 and 0.102 nm respectively, averaged across ten locations) with some vertical development (bright spots). **c**, MoS_2 surface after PDA treatment. Mean roughness across ten locations without crossing an edge is Ra: 0.060 nm and Rq: 0.075nm. Sapphire surface modification under the TMD monolayer into uniform double steps. **d**, Analysis of XZ line scans taken orthogonally to sapphire step edges before MoS_2 growth (after pretreatment/before nucleation) and after MoS_2 growth/PDA indicate that sapphire single steps coalesce into uniform double steps underneath the TMD overlayer during the PDA. **e**, Schematic representation of Al_2O_3 bulk unit cell and single/double stepped sapphire.

Figure 3



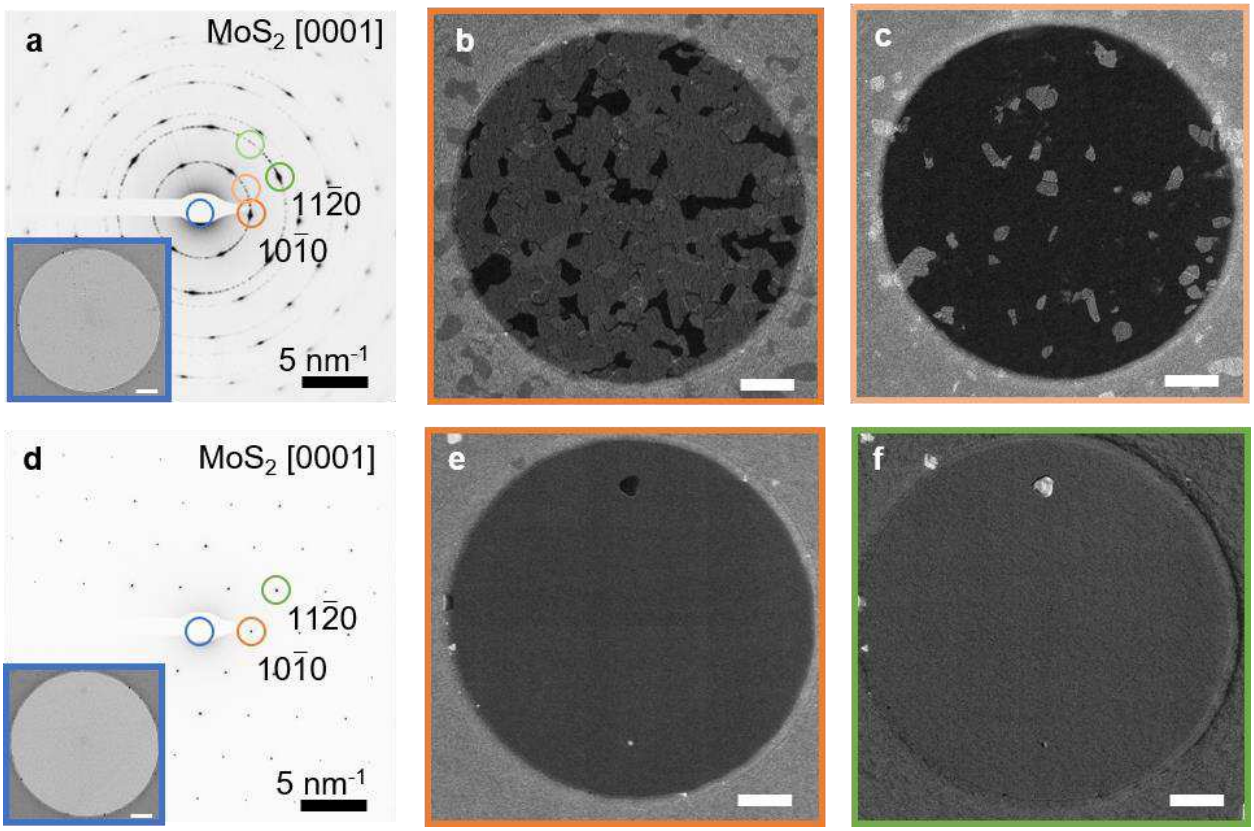
a, HAADF-STEM cross-sectional image of a MoS_2 monolayer deposited on a sapphire substrate and treated with a PDA. The gap between the two is attributed to a vdW buffer zone. **b**, Molybdenum signal in EDS map of monolayer MoS_2 on sapphire cross section. **c**, Sulfur signal in EDS map of monolayer MoS_2 on sapphire cross section. **d**, HAADF-STEM cross sectional image of a MoS_2 monolayer crossing a sapphire terrace double step. An apparent reduction in the vdW buffer zone can be seen as the monolayer approaches the edge of the terrace. **e**, Aluminum signal in EDS map of monolayer MoS_2 on sapphire cross section. **f**, Oxygen signal in EDS map of monolayer MoS_2 on sapphire cross section

Figure 4



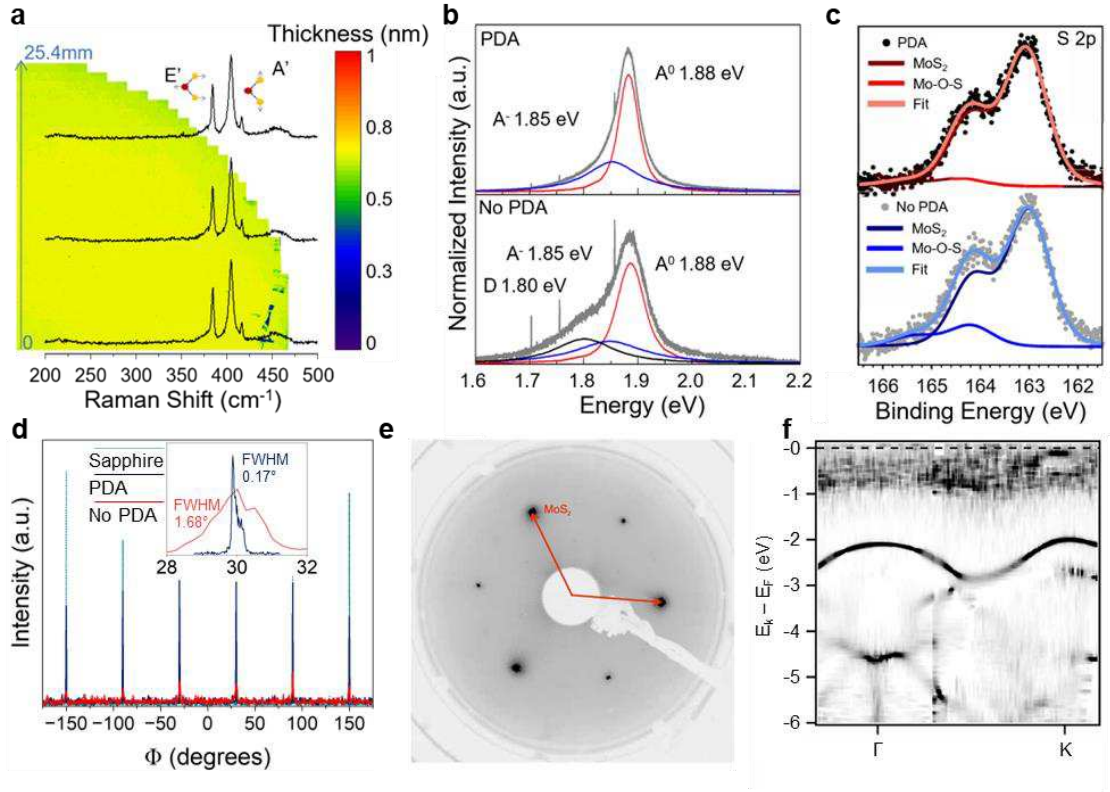
a, 500 x 500 nm AFM topography of a fully grown MoS_2 monolayer before PDA application showing meandering sapphire terraces edges overlaid with somewhat rough, granular MoS_2 surface. **b**, Co-localized C-AFM micrograph of current measurement for the region in panel a. Areas depicted in pink (yellow) indicate lower (higher) currents. Suspected high angle grain boundaries are revealed where current is highest. **c**, 75 x 75 nm C-AFM of region denoted by red box in panel b. **d**, 500 x 500 nm AFM topography of MoS_2 after PDA. Sapphire steps are smooth and uniform below a featureless, pristine MoS_2 monolayer. **e**, Co-localized C-AFM micrograph of current measurement for the region in panel d showing the absence of grain boundaries. **f**, 75 x 75 nm C-AFM of region denoted by red box in panel e.

Figure 5



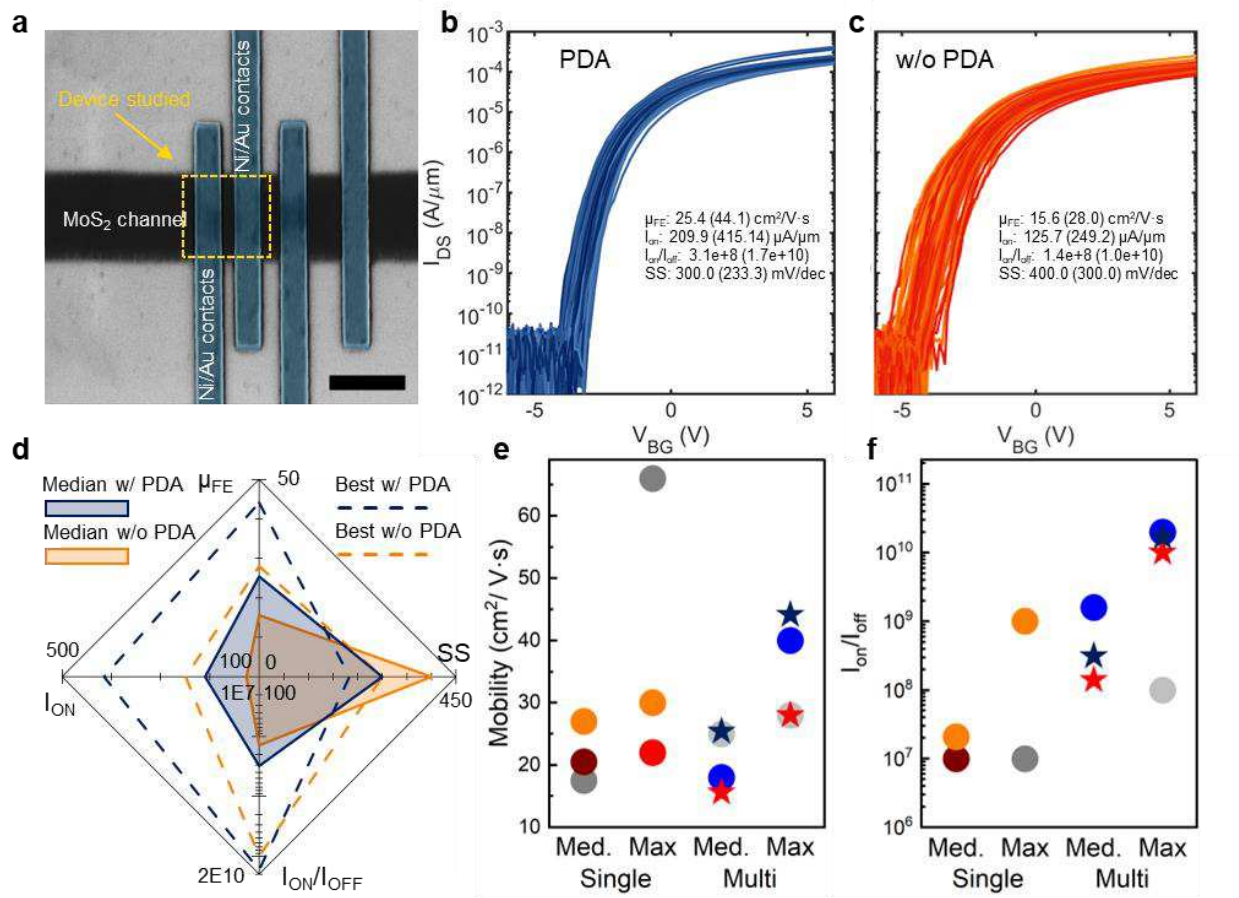
a, SAED and (inset) brightfield TEM image of fully grown monolayer without PDA treatment. Dark field TEM image of same layer taken on **b**, oriented and **c**, misoriented $10\bar{1}0$ showing special distribution of misoriented TMD grains. **d**, SAED and (inset) brightfield TEM image of fully grown monolayer after PDA treatment. Dark field TEM images of PDA treated layer taken on **e**, $10\bar{1}0$ and **f**, $11\bar{2}0$ spots. All white scale bars are 200 nm to include the brightfield inset. Dark field TEM images on $11\bar{2}0$ from the untreated layer are available in **Supplementary Figure 6**.

Figure 6



a, ISE map of a quarter of a 2” wafer indicating homogeneous monolayer MoS_2 thickness overlaid with Raman spectra taken at wafer center, half radius and edge. Spacing of primary in-plane and out-of-plane vibrational modes is consistent with a MoS_2 monolayer. **b**, Comparison of PL spectra from MoS_2 monolayers after (top) and before (bottom) PDA treatment. For both samples the neutral and negatively charged exciton contributions are found in appropriate locations, but on the sample that did not receive a PDA, an additional defect-associated shoulder is present. **c**, XPS data comparing the S 2p spectra of samples before (grey dots) and after (black dots) PDA. The area of the high-binding energy doublet - which is associated with defective sites – is reduced from >14% to <6% as a result of PDA. **d**, In-plane XRD measurements showing the degree of epitaxial registry between the MoS_2 and sapphire substrate, with and without PDA. Inset: FWHM of the MoS_2 peak after PDA is ten times narrower than that of MoS_2 before PDA. **e**, LEED pattern of MoS_2 on sapphire recorded with a primary beam energy of 95 eV. **f**, ARPES curvature plot of the band structure collected using He I light at 21.2 eV. The onset of the conduction band is visible in K as an increase of intensity near the Fermi level.

Figure 7



a, False colored scanning electron microscope (SEM) top-view images of a MoS_2 field-effect transistor. The yellow box highlights the channel region of this representative device with channel length (L_{ch})~200 nm(scale bar = 1 μm). **b**, Transfer curves from FET devices fabricated from MoS_2 films that underwent PDA treatment. **c**, Transfer curves from FET devices fabricated from MoS_2 films that did not undergo PDA treatment. **d**, Median and maximum measurements of four important device metrics (field effect mobility, subthreshold slope, on/off ratio and on state current) comparing PDA and non-PDA MoS_2 FET devices. **e**/**f**, Mobility benchmarks against specifically MOCVD growth on unmodified (except annealing) sapphire substrates. Blue and red stars are this work with and without PDA respectively. Circles represent data adapted from refs. 19 (red), 25 (dark red), 35 (blue), 43 (light grey), 56 (grey), 78 (orange).

Supplementary Files

This is a list of supplementary files associated with this preprint. Click to download.

- MCurtisSISubmissionv2CooperativeReconstructiveEpitaxyofMoS2MonolayersinaMultiWaferMOCVDProcessGuidedbyInSituProcessMonitoring.pdf